

Probing the 2D temperature structure of protoplanetary disks with *Herschel* observations of high- J CO lines

D. Fedele^{1,2}, E.F. van Dishoeck^{2,3}, M. Kama³, S. Bruderer², M.R. Hogerheijde³

¹ INAF-Osservatorio Astrofisico di Arcetri, L.go E. Fermi 5, I-50125 Firenze, Italy,

² Max Planck Institut für Extraterrestrische Physik, Giessenbachstrasse 1, 85748 Garching, Germany,

³ Leiden Observatory, Leiden University, P.O. Box 9513, NL-2300 RA, Leiden, The Netherlands

October 19, 2018

ABSTRACT

The gas temperature structure of protoplanetary disks is a key ingredient for interpreting various disk observations and for quantifying the subsequent evolution of these systems. The comparison of low- and mid- J CO rotational lines is a powerful tool to assess the temperature gradient in the warm molecular layer of disks. Spectrally resolved high- J ($J_u > 14$) CO lines probe intermediate distances and heights from the star that are not sampled by (sub-)millimeter CO spectroscopy. This paper presents new *Herschel*/HIFI and archival PACS observations of ^{12}CO , ^{13}CO and [C II] emission in 4 Herbig Ae/Be (HD 100546, HD 97048, IRS 48, HD 163296) and 3 T Tauri (AS 205, S CrA, TW Hya) disks. In the case of the T Tauri systems AS 205 and S CrA, the CO emission has a single-peaked profile, likely due to a slow wind. For all other systems, the *Herschel* CO spectra are consistent with pure disk emission and the spectrally-resolved lines (HIFI) and the CO rotational ladder (PACS) are analyzed simultaneously assuming power-law temperature and column density profiles, using the velocity profile to locate the emission in the disk. The temperature profile varies substantially from disk to disk. In particular, T_{gas} in the disk surface layers can differ by up to an order of magnitude among the 4 Herbig Ae/Be systems with HD 100546 being the hottest and HD 163296 the coldest disk of the sample. Clear evidence of a warm disk layer where $T_{\text{gas}} > T_{\text{dust}}$ is found in all the Herbig Ae disks. The observed CO fluxes and line profiles are compared to predictions of physical-chemical models. The primary parameters affecting the disk temperature structure are the flaring angle, the gas-to-dust mass ratio the scale height and the dust settling.

Key words. Protoplanetary disks – Stars: formation

1. Introduction

A key physical parameter of protoplanetary disks is the gas temperature, T_{gas} . Inside a disk T_{gas} controls the dynamics of the gas by setting the sound speed and, through that, also the disk photoevaporation. At the same time T_{gas} governs the chemical composition by regulating the reaction rates between different species. Disks are characterized by a strong temperature gradient both in the radial and vertical directions. For this reason, multiple transitions, tracing different vertical layers and different orbital radii, have to be observed to derive T_{gas} in disks. An ideal disk ‘thermometer’ is the CO rotational ladder. Low- J ($J_u < 6$) CO rotational lines are routinely observed from the ground in protoplanetary disks since the late 90s (e.g., Koerner & Sargent 1995; Mannings & Sargent 1997; Dutrey et al. 1998; van Zadelhoff et al. 2001). These lines probe mostly the cold gas in the outer disk ($r > 100$ au). Recent observations of disks with *Herschel*/PACS carried out by the DIGIT (Green et al. 2013) and GASPS (Dent et al. 2013) key programs report the detection of pure rotational high- J ($J_u > 14$) CO emission lines (e.g., Sturm et al. 2010; van Kempen et al. 2010; Meeus et al. 2012, 2013). These lines trace warm gas ($E_u \geq 300$ K) located in intermediate layers between the disk surface and the midplane at intermediate distances from the star (10 – 50 au) as predicted by

thermo-chemical models of UV irradiated disks (e.g., Jonkheid et al. 2007; Gorti & Hollenbach 2008; Woitke et al. 2009; Kamp et al. 2010; Bruderer et al. 2012).

The detections of the CO high- J lines allow us, for the first time, to estimate the gas temperature in this region of the disk. However, the PACS spectra (resolving power $R = \lambda/\Delta\lambda \sim 10^3$) presented by Meeus et al. (2013) are spectrally and spatially unresolved, so that their emitting region (hence, the radial distribution of the gas) can only be inferred indirectly from the modeling of line fluxes (e.g. Bruderer et al. 2012). The only way to overcome the lack of spatial resolution at high THz frequencies, and to determine the warm gas distribution within disks is with high-resolution spectroscopy with HIFI ($R = 10^6 - 10^7$), where Kepler’s law can be used to associate a velocity bin with a radial location in the disk.

The *Herschel* PACS and HIFI CO spectra of the Herbig Ae system HD 100546 have been presented in Fedele et al. (2013b) (hereafter paper I) in which the radial gas temperature gradient is estimated for the first time. This paper presents new *Herschel*/HIFI observations of CO $J = 16 - 15$ toward: HD 97048, AS 205, Oph-IRS 2-48 and S CrA, CO and ^{13}CO $J = 10 - 9$ toward TW Hya, HD 100546 and HD 163296. *Herschel*/HIFI observations of [C II] (158 μm) in HD 97048 and HD 100546 are reported in the Appendix.

Send offprint requests to: Davide Fedele,
e-mail: fedele@mpg.de

Table 1. *Herschel*/HIFI observations log and line properties.

Target	RA (J2000)	DEC (J2000)	Obsid 13422-	v_{LSR} [km s ⁻¹]	FWHM [km s ⁻¹]	rms [K]	dv [km s ⁻¹]	Int. Intensity [K km s ⁻¹]	Int. Flux [10 ⁻¹⁷ W m ⁻²]
CO $J = 16 - 15$, $E_u = 751.8$ K, 1841.345 GHz, $\eta_{\text{mb}} = 0.57$ (H), 0.60 (V), HPBW = 11.1''									
HD 97048	11:08:03.32	-77:39:17.5	50973	4.9	7.4	0.04	0.08	1.42 ± 0.05	2.97 ± 0.10
HD 100546	11:33:25.44	-70:11:41.2	47519	5.3	8.2	0.06	0.08	2.89 ± 0.08	6.06 ± 0.17
AS 205	16:11:31.40	-18:38:24.5	51072	4.8	3.7	0.04	0.08	0.76 ± 0.06	1.59 ± 0.12
Oph-IRS 48	16:27:37.19	-24:30:35.0	51070	4.8	12.0	0.04	0.08	0.40 ± 0.04	0.84 ± 0.08
S CrA	19:01:08.60	-36:57:20.0	53691	6.4	2.6	0.04	0.08	1.35 ± 0.07	2.83 ± 0.15
CO $J = 10 - 9$, $E_u = 304.2$ K, 1151.985 GHz, $\eta_{\text{mb}} = 0.59$ (H), 0.59 (V), HPBW = 19.5''									
TW Hya	11:01:51.91	-34:42:17.0	10733	2.9	1.3	0.06	0.13	0.22 ± 0.04	0.34 ± 0.06
HD 100546	11:33:25.44	-70:11:41.2	35779	5.5	6.4	0.04	0.13	3.29 ± 0.05	5.21 ± 0.08
HD 163296	17:56:21.29	-21:57:21.9	51440	5.9	6.5	0.07	0.13	0.95 ± 0.23	1.51 ± 0.37
¹³ CO $J = 10 - 9$, $E_u = 290.8$ K, 1101.349 GHz, $\eta_{\text{mb}} = 0.59$ (H), 0.59 (V), HPBW = 19.5''									
TW Hya	11:01:51.91	-34:42:17.0	01585	2.7	1.2	0.006	0.14	0.02 ± 0.003	0.028 ± 0.004
HD 100546	11:33:25.44	-70:11:41.2	56430	5.5	7.8	0.007	0.14	0.64 ± 0.03	0.88 ± 0.06
HD 163296	17:56:21.29	-21:57:21.9	53595	5.9	9.5	0.006	0.14	0.14 ± 0.01	0.19 ± 0.01
[C II] ² P _{3/2} ⁰ - ² P _{1/2} ⁰ , $E_u = 91.3$ K, 1900.537 GHz, $\eta_{\text{mb}} = 0.57$ (H), 0.60 (V), HPBW = 11.1''									
HD 97048	11:08:03.32	-77:39:17.5	52194	4.90	2.75	0.10	0.08	4.09 ± 0.09	9.44 ± 0.21
HD 100546	11:33:25.44	-70:11:41.2	47518	5.75	3.70	0.09	0.08	8.50 ± 0.15	19.6 ± 0.34

Notes. The rms is measured at the original spectral resolution, channel width given in column “dv”.

2. Observations and data reduction

The sample selection is based on the PACS detection of high- J CO and [C II] emission (Meeus et al. 2013; Fedele et al. 2013a). The observations log is reported in Table 1. Most of the data are taken from program ID OT2_DFedele_1 (PI: D. Fedele). The HIFI ¹²CO and ¹³CO $J = 10 - 9$ spectra are obtained from the WISH key program (PI: E.F. van Dishoeck) for TW Hya, and from programs OT1_mhogerhe_1 (HD 100546 ¹²CO $J = 10 - 9$, PI: M. Hogerheijde), OT2_mhogerhe_2 (HD 100546 and HD 163296 ¹³CO $J = 10 - 9$, PI: M. Hogerheijde) and OT1_lpodio_1 (HD 163296 ¹²CO $J = 10 - 9$, PI: L. Podio).

The CO observations were executed in dual beam switch fast chopping mode with the Wide-Band Spectrometer (WBS) and the High Resolution Spectrometer (HRS) simultaneously. The spectral resolution is set to 1.1 MHz for WBS and 0.25 MHz for HRS for both polarizations. The [C II] observations were carried out in ‘load chop’ where an internal calibration source is used in combination with an off-source calibration observation. This allows us to remove the spatially extended [C II] emission. The beam size (HPBW) is 11'1 at the observed frequency (Roelfsema et al. 2012). In the following, we will refer only to the WBS spectra.

The spectra are extracted from the level 2 data which have been processed with standard pipeline SPG v9.1.0. Standing waves are present in the WBS spectra. These have been removed by fitting a set of sine functions after masking the narrow spectral features (CO or [C II]). This operation was performed with the ‘fitHifiFringe’ script provided with Hipe. The HIFI level 2 fluxes are given on the antenna temperature scale (T_A^*). These are converted to main beam temperature, $T_{\text{mb}} = T_A^* \times \eta_l / \eta_{\text{mb}}$, with η_l

the forward efficiency and η_{mb} the beam efficiency (Table 1). No major differences are present between the H and V polarizations and the two spectra are averaged together after applying the efficiency corrections and removing the continuum. High- J CO lines are not contaminated by the cold cloud contribution that plagues single dish low- J CO lines.

The reduction of the archival PACS data analysed here is described in Meeus et al. (2013) and Fedele et al. (2013a).

3. Results

The HIFI/WBS CO spectra are presented in Figure 1 and the line parameters are given in Table 1. The [C II] spectra and analysis is presented in the Appendix. The integrated line flux (W m⁻²) is computed from the integrated intensity

$$\int T_{\text{mb}} dV = 2k \left(\frac{\nu}{c}\right)^3 \pi \left(\frac{\text{HPBW}}{2\sqrt{\ln(2)}}\right)^2 \int T_{\text{mb}} dV \quad [\text{K km s}^{-1}] \quad (1)$$

with k (Boltzmann constant, W s K⁻¹), ν the frequency (Hz), c the light speed (m s⁻¹) and HPBW the beam (radians). Note that because of the updated values of the beam efficiency (Table 1), the line intensities presented here for HD 100546 are slightly different (~ 3 %) from the values given in paper I.

The top panel of Figure 1 shows the WBS spectra of the CO $J = 16 - 15$ lines toward HD 97048, HD 100546, IRS 48, AS 205 and S CrA. The line is clearly detected above 5 σ (Table 1) in all sources. The velocity profile and width are different among the five sources. The emission is broad ($\Delta v > 5$ km s⁻¹) toward the

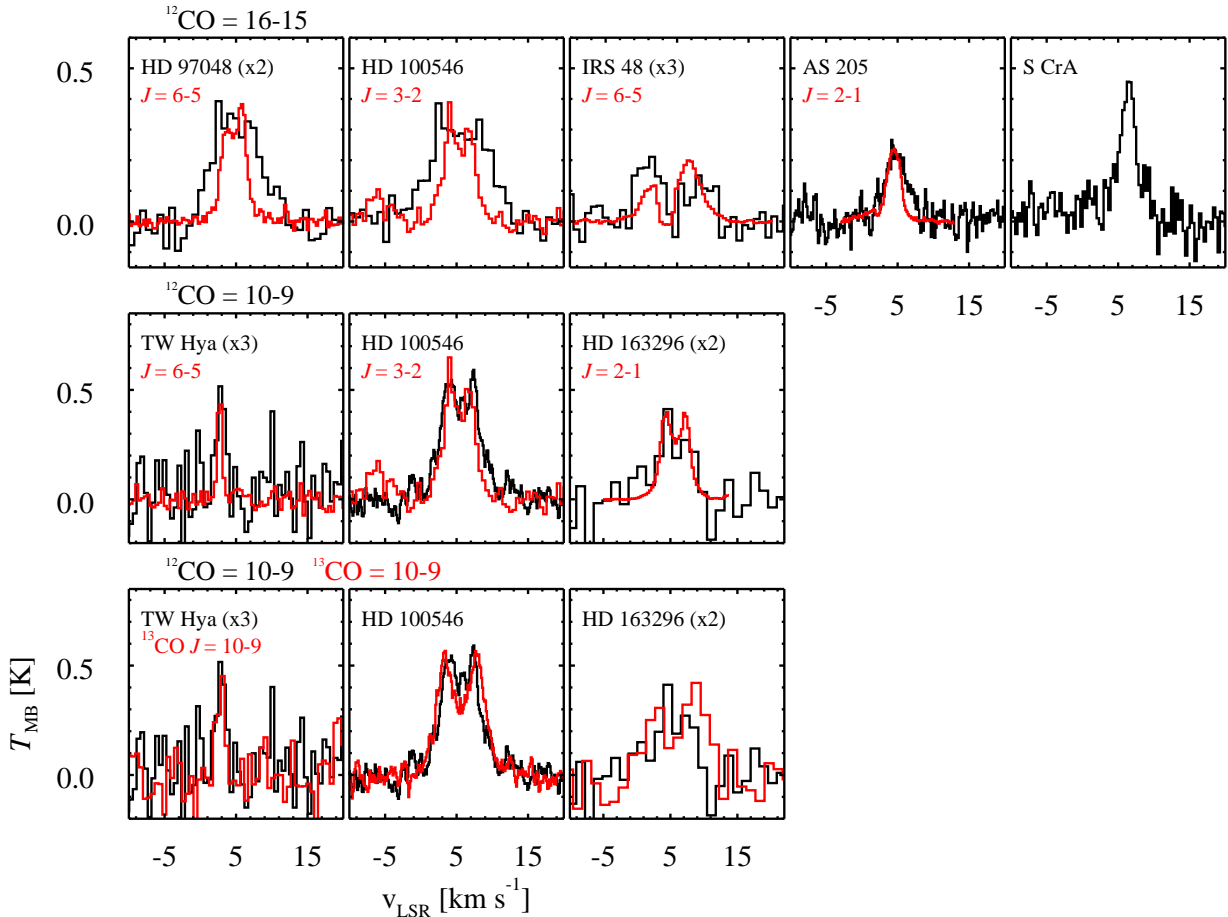


Fig. 1. HIFI/WBS spectra of CO $J=16-15$ (top), $J = 10 - 9$ (middle and bottom) and $^{13}\text{CO } J = 10 - 9$ (bottom). The spectra of low- J lines are overlaid in red (scaled for comparison) in top and middle rows. For clarity, some spectra are rebinned to lower resolution: for CO $J = 16 - 15$ $\text{d}v = 0.8 \text{ km s}^{-1}$ in HD 97048, HD 100546 and IRS 48 and $\text{d}v = 0.32 \text{ km s}^{-1}$ in S CrA; for CO $J = 10 - 9$ $\text{d}v = 0.52 \text{ km s}^{-1}$ in TW Hya and $\text{d}v = 1.3 \text{ km s}^{-1}$ in HD 163296; for $^{13}\text{CO } J = 10 - 9$ $\text{d}v = 0.56 \text{ km s}^{-1}$ in TW Hya and $\text{d}v = 1.4 \text{ km s}^{-1}$ in HD 163296. The remaining spectra are shown at their native resolution.

three HAeBe stars HD 97048, HD 100546 and IRS 48: a double-peak profile is clearly visible in HD 100546 and IRS 48, while the CO velocity profile is top-flat in HD 97048. In all three cases, the WBS spectra of the CO $J = 16 - 15$ transition are consistent with a Keplerian velocity field of the gas in the disk. In the case of the two T Tauri systems, AS 205 and S CrA, the CO $J = 16 - 15$ emission is narrow ($\Delta v < 5 \text{ km s}^{-1}$) and single-peaked. There is no evidence of Keplerian rotation. For comparison, the profiles of the low- J CO lines are also shown when available. Spectra (either APEX or ALMA) are from Panić et al. (2010); Bruderer et al. (2014); Salyk et al. (2014) and Kama et al. (in prep.). In all cases, the low and high- J CO lines are centered at the same v_{LSR} with the CO $J = 16 - 15$ line broader than the low- J one. Note that part of the asymmetric profile of the $J = 6 - 5$ line toward IRS 48 is due to extinction from the foreground cloud (Bruderer et al. 2014). In the case of AS 205 both CO lines are centered at $v_{\text{LSR}} = 4.8 \text{ km s}^{-1}$ compared to the cloud velocity of $v_{\text{LSR}} = 3 \text{ km s}^{-1}$. Thus we conclude that the high- J CO emission in AS 205 arises from a slow wind/outflow similarly to the low- J CO (Salyk et al. 2014) and to the ro-vibrational (Pontoppidan et al. 2011) emission.

The narrow, single-peak, profile of the CO $J = 16 - 15$ emission in S CrA suggests also a contribution from a slow wind associated to the system. The CO ro-vibrational lines toward both stellar components in this binary are broad and single-peaked, similar to AS 205 (Bast et al. 2011; Brown et al. 2013).

Figure 1 also shows the HIFI/WBS spectra of CO $J = 10 - 9$ compared to the low- J transitions (middle) and to the ^{13}CO (bottom) for TW Hya, HD 100546 and HD 163296. Both the ^{12}CO and ^{13}CO lines are clearly detected. The lines are broad and double-peaked toward HD 100546 and HD 163296 and narrow and single-peaked toward TW Hya. In all 3 cases, the lines are centered on the system velocity and the narrow line profile of TW Hya is consistent with the disk being almost face-on to the plane of the sky. As noted in paper I, the line width is narrower for lower J transitions in HD 100546. In the case of HD 163296 instead, the width of the $J = 2 - 1$ (ALMA science verification data) and $J = 10 - 9$ are similar. Note that the ^{12}CO and $^{13}\text{CO } J = 10 - 9$ profiles appear asymmetric toward HD 163296, however the flux difference between the two peaks is within the noise level of the spectrum.

Interestingly, the ^{13}CO line toward HD 100546 and HD 163296 is slightly broader than the ^{12}CO one (Figure 1, bottom row).

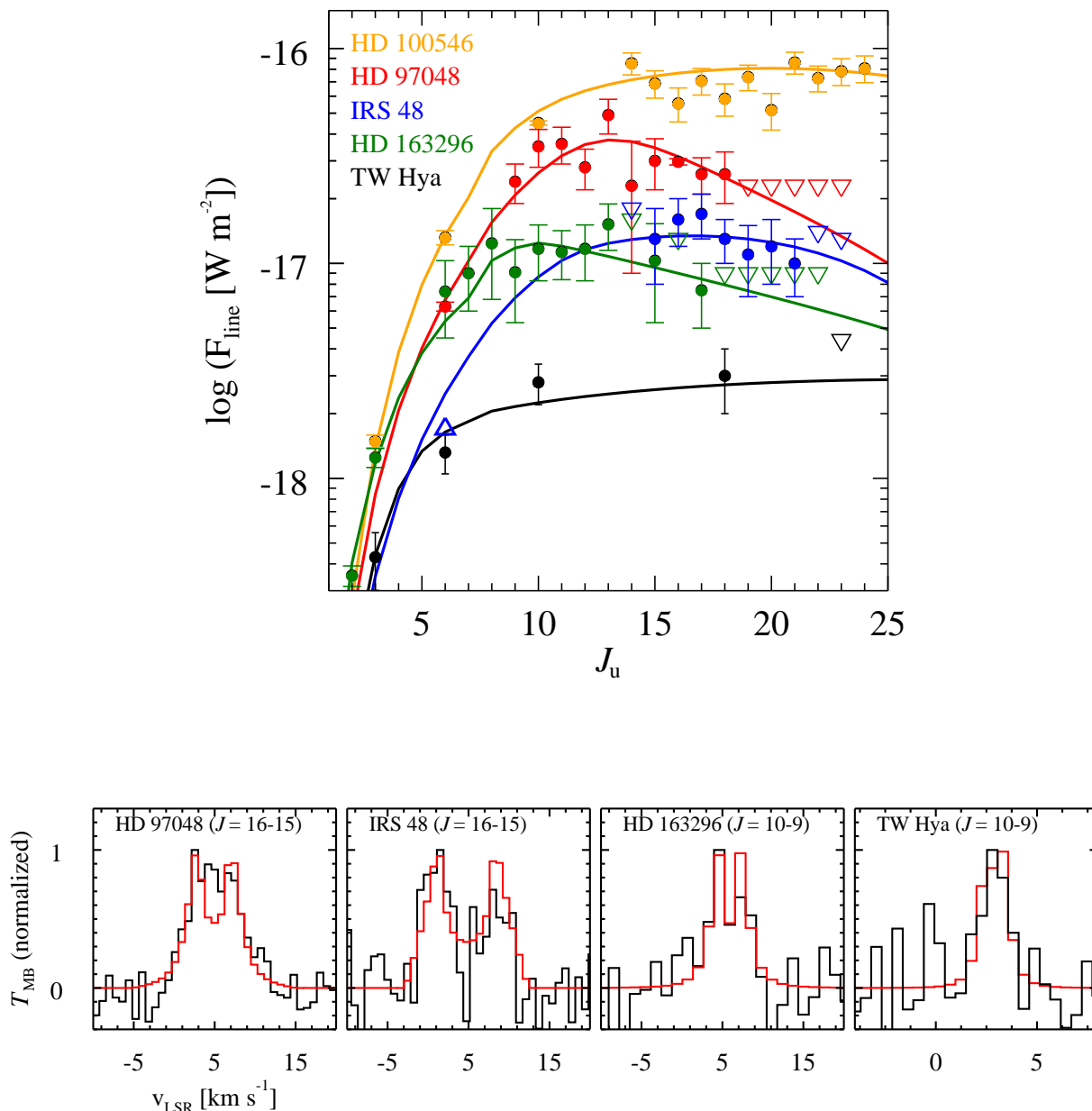


Fig. 2. (top) CO rotational ladder. Detections are shown as filled circles and upper limits as open triangles. The solid lines represent the best-fit power-law model. (bottom) Best-fit model profile of the CO $J = 16 - 15$ (HD 97048 and IRS 48) and CO $J = 10 - 9$ (HD 163296 and TW Hya). Spectral resolution as in Figure 1.

This implies that the line emitting region of ^{13}CO extends to higher velocity regions, i.e. closer to the star. Another prominent difference is the central peak detected in the ^{12}CO $J = 10 - 9$ line in the HD 100546 spectrum which is not visible in the ^{13}CO spectrum. The differences in the velocity profiles are likely due to optical depth effects: the ^{12}CO line becomes optically thick at lower column densities, higher up in the atmosphere, than the ^{13}CO line. This is discussed further in section 5.

4. Analysis

The CO rotational ladder is a powerful tool to assess the temperature structure of protoplanetary disks (Bruderer et al. 2012; Fedele et al. 2013b; van der Wiel et al. 2014). The low- J lines are optically thick and the lines become optically thin only at $J_u \gtrsim 14$ (Bruderer et al. 2012). The advantage of the high- J CO rotational lines is that they trace intermediate distances from the star (a few tens of au) and heights ($z/r \sim 0.1 - 0.4$) above the disk midplane. The high- J CO transitions are complementary to the low- J CO transitions observed at millimeter observations which trace the colder outer disk. Thus the flux and velocity profile of

Table 2. Best-fit power-law model parameters

	TW Hya	HD 97048	HD 100546 [†]	HD 163296	IRS 48
M_{\star} (M_{\odot})	0.6	2.5	2.5	2.4	2.0
d (pc)	51	180	97	120	120
i ($^{\circ}$)	7	43	42	44	50
r_i (au)	0.1	11	13	0.1	20
r_{out} (au)	200	400	400	600	200
T_i (K)	3000 – 5000	500 – 600	750-1450	1000 – 1100	250 – 350
q	0.7 – 0.8	0.5 – 0.6	0.75 – 0.95	0.5 – 0.6	0.85 – 0.95
N_i (cm^{-2})	$1 - 5 \times 10^{18}$	$10^{18} - 10^{19}$	$2 - 8 \times 10^{-17}$	$10^{19} - 10^{20}$	$10^{18} - 10^{19}$
p	0.85 – 0.95	0.45 – 0.55	0.6-1.2	0.3 – 0.35	0.55 – 0.65

Notes. ^(†) From paper I. Best fit parameters are found by χ^2 minimization. Ranges represent the 1- σ interval.

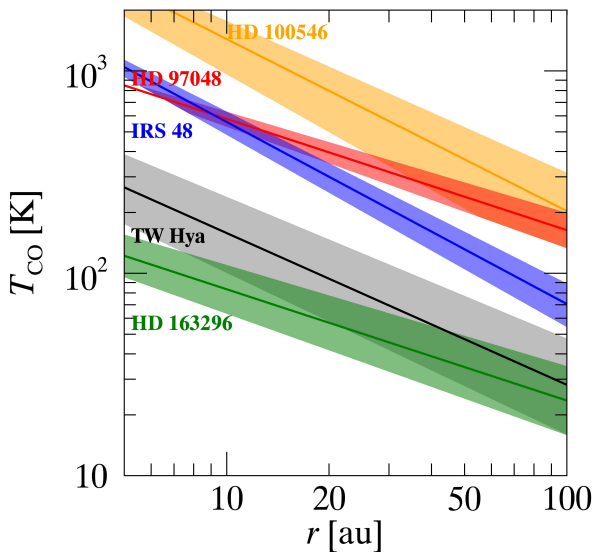


Fig. 3. CO temperature profile in the inner 100 au based on the best-fit power-law models (Table 2).

the high- J CO lines are crucial to measure the gas temperature in the disk atmosphere. The rotational ladder (Table A.1) is compiled combining low- J lines ($J_u < 6$) from ground based observations, mid- J ($J_u = 7 - 12$) from SPIRE (van der Wiel et al. 2014) and high- J ($J_u > 14$) lines from *Herschel*/PACS (Meeus et al. 2013). In some cases, the CO line fluxes measured with SPIRE are contaminated by extended emission (cloud) as noted by van der Wiel et al. (2014). The lines which are affected are excluded from the fit.

The CO rotational ladders for the 5 disks are shown in Figure 2. The shape of the ladder varies from object to object. Note in particular the difference between HD 100546 and HD 163296: in the first case the CO line flux increases with J and then it remains almost constant while in the case of HD 163296, the rotational ladder turns over at $J_u \sim 10 - 15$.

The analysis of HD 100546 is presented in paper I. The sources AS 205 and S CrA are excluded from this analysis because the CO line fluxes and velocity profiles are dominated by an outflow/jet.

4.1. Power-law model

Following the method described in paper I the CO rotational ladder and the line velocity profiles ($J = 16 - 15$ for HD 97048 and IRS 48, $J = 10 - 9$ for TW Hya and HD 163296) are fitted simultaneously using a power-law profile for the kinetic gas temperature (under the assumption that the CO excitation temperature corresponds to the kinetic temperature, which is valid given the high densities of the emitting regions) and column density:

$$T(r) = T_i \left(\frac{r}{r_i} \right)^{-q} \quad (2)$$

$$N(r) = N_i \left(\frac{r}{r_i} \right)^{-p} \quad (3)$$

where T_i and N_i are the values at the inner radius r_i of the disk (fixed, Table 2). The stellar and disk parameters are taken from literature. In particular $r_i = 0.1$ au for TW Hya (Pontoppidan et al. 2008), 13 au for HD 100546 (van der Plas et al. 2009; Brittain et al. 2009; Fedele et al. 2015), 11 au for HD 97048 (van der Plas et al. 2009) and 20 au for IRS 48 (Bruderer et al. 2014). The power-law is truncated at the outer disk radius, r_{out} (fixed, Table 2, the choice of the outer radius does not matter as long as $r_{\text{out}} > 100$ au). The free parameters of the model are: T_i , q , N_i , p . A grid of models is created for each disk varying the 4 parameters in the ranges: $T_i = 300 - 1500$ K, $N_i = 10^{17} - 10^{22}$ cm^{-2} , $q, p = 0.5 - 1.5$. The spectra are spatially convolved with the telescope beam, represented here by a Gaussian profile. Further details about the model and the fitting procedure are given in paper I. The best-fit parameters are found by minimizing the χ^2 between observations and model. The final χ^2 is given by the sum of the individual χ^2 of the CO rotational ladder and of the line profiles (one for each line), including their width and peak separation. The best-fit model parameters are listed in Table 2 and the best-fit models are overlaid on the data in Figure 2.

The derived temperature profiles (labeled T_{CO}) are plotted in Figure 3. Evidence of warm disk temperature ($T > 100$ K) is found for HD 97048, HD 100546 and IRS 48. The coldest disks are TW Hya and HD 163296 both having $T < 100$ K outward of 20 au.

4.2. Caveats of the power-law model

The assumption of a flat disk geometry is justified by the results of physical-chemical models that predict that most of the CO rotational lines arise from a similar vertical layer in the disk.

Table 3. DALI model parameters for Herbig Ae disks

Parameter	Value	Unit	Description
M_\star	2	$[M_\odot]$	Stellar mass
T_{eff}	8000, 9000 , 10500	[K]	Stellar (blackbody) temperature
L_{bol}	20	$[L_\odot]$	Bolometric luminosity
$\Delta_{\text{gas/dust}}$	1, 10 , 100		Gas-to-dust mass ratio
PAHs	1 , 10, 50	[% (w.r.t. ISM)]	PAHs abundance
M_{disk}	10^{-4} , 10^{-3} , 10^{-2}	$[M_\odot]$	Disk mass
γ	0.8, 1 , 1.2		Surface density power-law exponent
R_{sub}	0.31	[au]	Sublimation radius
R_c	50, 75 , 100	[au]	Critical radius
h_c	0.1, 0.2 , 0.3	[radians]	Scale height
R_{out}	200, 400 , 600	[au]	Disk outer radius
ψ	0.05 , 0.15, 0.25		Flaring angle
χ	0.2 , 0.5, 1.0		Degree of settling
f_{large}	0.50, 0.85 , 0.999		Large-to-small grains mass ratio
a_{min}	0.001 , 0.01, 0.05	$[\mu\text{m}]$	Minimum grain size
L_X	10^{29}	$[\text{erg s}^{-1}]$	X-rays luminosity
d	100	[au]	Distance
i	45	$[\circ]$	Disk inclination

Notes. Values in bold face indicate the representative disk models. For model description and parameters definition see Bruderer (2013).

With this assumption however, the power-law model fails to reproduce the core of the line profile, especially in the case of HD 97048 (Figure 2) where the line wings are well reproduced by the model while the central low velocity part of the line is not. This can be due to an optical depth effect (if the core of the line is optically thick) or to a geometrical effect. In this case indeed, given the disk inclination (43°), the core of the line in the *Herschel* beam may be filled-in by emission coming from the back side of the disk as found for the lower J CO lines from ALMA data by de Gregorio-Monsalvo et al. (2013).

The second major caveat of the power-law model is that the column density profile is not constrained: most of the lines are optically thick and the CO ladder is mostly sensitive to the temperature profile of the $\tau_{\text{line}} = 1$ layer. Thus, even if N_{in} and p are free parameters of the model, these values are to be taken with caution.

5. Comparison to disk models

The goal of this section is to explain the large variation in the CO rotational ladder and velocity profiles among Herbig Ae systems (Figures 1 and 2). This study is based on the physical-chemical model DALI (Bruderer et al. 2012; Bruderer 2013). DALI takes as input a density structure of the disk (taken to be a power-law with slope γ and critical radius R_c , with an exponential tail) and a stellar radiation field, then solves the continuum radiative transfer and determines the dust temperature and ultraviolet radiation field at each position in the disk. Thermal balance of the gas and chemistry are subsequently solved iteratively until convergence. The output includes: continuum and line emission maps, line intensities and spectra produced via ray tracing. Dust settling is included adopting two grain size populations, small ($a_{\text{min}} - 1 \mu\text{m}$) and large (1 - 1000 μm) following D’Alessio et al. (2006) and dust cross sections from Andrews et al. (2011). The degree of settling of the large grains is controlled in DALI by the parameters χ and f_{large} : the first defines the maximum scale height of the large grains with respect to the small ones (similar to “ Z_{big} ” in D’Alessio et al. 2006), while f_{large} determines the small-to-large grains mass ratio.

Figure 4 shows the gas density (top row) structure for the two representative models (Table 3, the spectral energy distribution of the two models is shown in Appendix). The inset shows the inner disk structure. The line contribution functions of a set of low- J and high- J transitions of ^{12}CO and ^{13}CO are overlaid on the n_{gas} contours showing the layer where 50% of the line flux emerges. The CO emitting layer varies slightly with J and the four transitions shown here emerge from a layer between $z/r \sim 0.4 - 0.6$ and $z/r \sim 0.3 - 0.5$ for the flat and flared disk, respectively. In all cases, the ^{13}CO lines emerge closer to the disk midplane and at smaller stellar distances compared to the ^{12}CO lines; because of the vertical and radial density gradients, the CO emission becomes optically thick higher up in the disk atmosphere and at larger distance from the star compared to the ^{13}CO line. This is in excellent agreement with the broader velocity profile observed for ^{13}CO (Table 1, Figure 1, bottom row).

The gas temperature structure for the representative models is shown in Figure 4 (middle panel). At any given position in the disk, the gas and dust temperatures increase with flaring angle. Note in particular that the dust temperature in both disks is $T_{\text{dust}} > 20 \text{ K}$ everywhere in the disk. This prevents CO from freeze-out on dust grains as condensation occurs only at $T \lesssim 20 \text{ K}$ in the disk interior. Without CO freeze-out, formation of complex species via surface chemistry is inhibited in such a warm disk. In both cases, T_{gas} is larger than T_{dust} in the upper layers of the disk.

The T_{gas} radial profile at different height (z/r) for the two representative models is shown in the bottom panel of Figure 4: in the flat disk case, the temperature increases slightly with height with an almost identical radial dependence from the disk midplane ($z/r = 0.01$) up to the disk upper layers. This is no longer true for flared disks which show a strong dependence of $T_{\text{gas}}(r)$ with disk height.

5.1. Disk models grid

This section provides a qualitative comparison to physical-chemical models of Herbig AeBe disks. For this, a grid of DALI disk models is built to study the impact of different stellar and

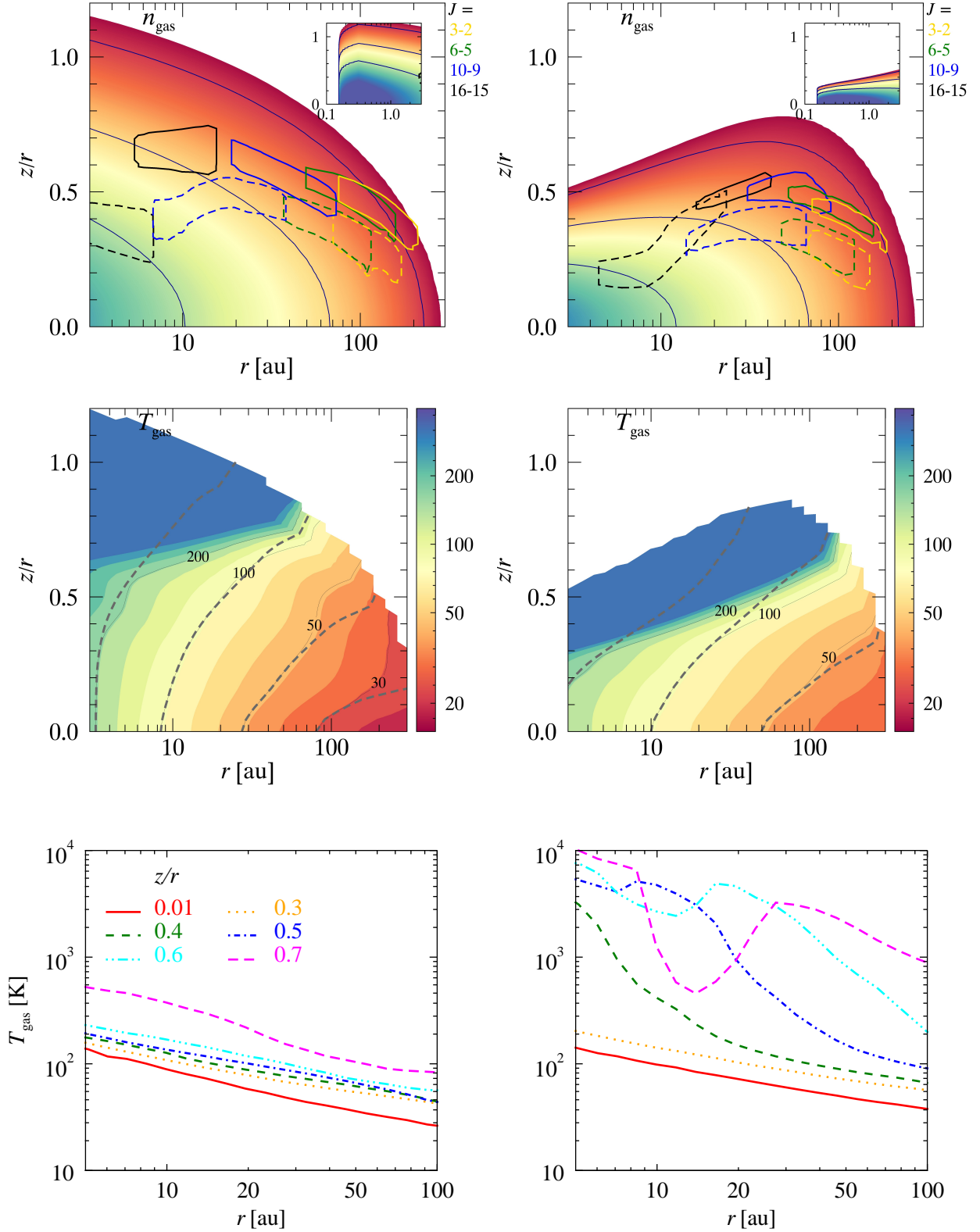


Fig. 4. DALI disk structure of the two representative models, $\psi = 0.05$ (left panels) and $\psi = 0.25$ (right panels). (Top) Gas density structure: the inset shows the inner disk structure, the dark-blue curves indicate the $n_{\text{gas}} = 10^6, 10^8$ and 10^{10} cm^{-3} contours. The line contribution functions of a mix of low- and high- J transitions of ^{12}CO (solid lines) and ^{13}CO (dashed) are overlaid on the n_{gas} panels. Each contour shows the layer where 50% of the line flux emerges. (Middle) Gas temperature structure, the isothermal contours are overlaid for T_{gas} and T_{dust} (dashed lines) = 20, 50, 100, 200 and 500 K. (Bottom) Gas temperature radial profile at different disk height relevant for the disk midplane ($z/r = 0.01$) and for the CO emitting layers.

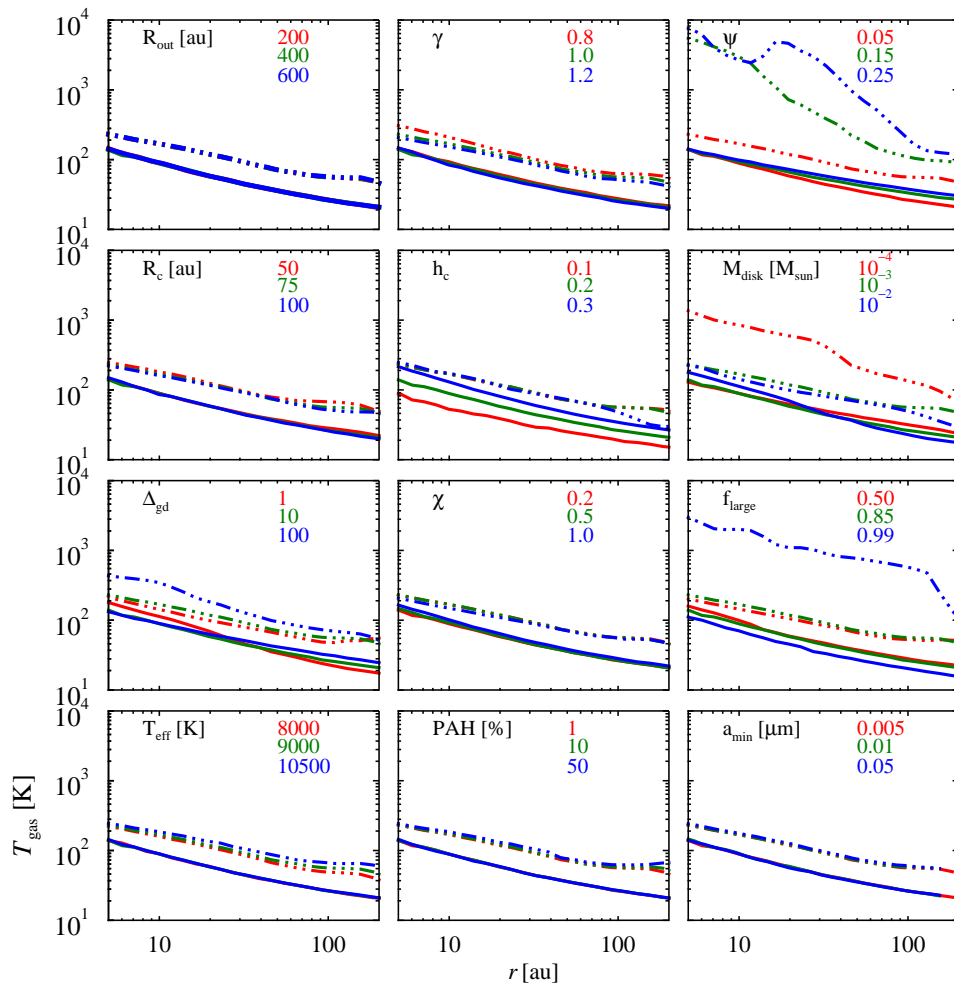


Fig. 5. T_{gas} radial profile for different disk/stellar parameters. The temperature radial profile is shown for the layers $z/r=0.01$ (solid lines) and 0.6 (dot-dashed lines). In the case of $h_c = 1$, the CO emitting layer is $z/r \sim 0.2 - 0.3$ and the dot-dashed line shows the temperature gradient at $z/r = 0.3$.

disk parameters on the disk thermal structure. The stellar mass and the bolometric luminosity are taken to be fixed while the stellar effective temperature (T_{eff} , assuming black body emission), the disk mass (M_{disk}), critical radius (R_c), disk outer radius (R_{out}), scale height (h_c), power-law exponent (γ), flaring angle (ψ), dust settling (χ, f_{large}), minimum grain size (a_{min}), gas-to-dust mass ratio (Δ_{gd}) and the PAH abundances are varied (Table 3). Several of these parameters were also investigated in Bruderer et al. (2012) but only for a flared disk. The model grid is built around the flat ($\psi = 0.05$) disk representative model varying the aforementioned parameters by the values given in (Table 3). In particular, the values of T_{eff} are representative of the typical stellar temperature of Herbig Ae systems (e.g., van den Ancker et al. 1998). The FUV (6 – 13.6 eV) luminosity, relevant for the heating of the disk and the photodissociation of CO, is regulated by T_{eff} and it ranges between $L_{\text{FUV}} = 0.45 - 1.7 L_{\odot}$ for $T_{\text{eff}} = 8,000 - 10,500$ K, respectively.

To investigate the impact of dust settling on the disk thermal structure, χ and f_{large} are varied between 0.2 – 1, 0 and 0.5 – 0.999, respectively (Table 3). Lowering the value of χ has the effect to let the UV photons penetrate further inside the disk. As a

consequence the $\text{C}^+/\text{C}/\text{CO}$ transition layers shift deeper into the disk. For $f_{\text{large}} = 0.5$ the dust mass is distributed equally between the small and the large dust grains, for $f_{\text{large}} = 0.999$, the bulk of the dust mass is in the large dust grains.

The abundance of PAHs and the gas-to-dust mass ratio are poorly constrained in disks. Model fits to observational data suggest PAH abundances that are typically 10-100 times lower than those in the interstellar medium (Geers et al. 2006). For Herbig AeBe disks, PAHs of about 100 carbon atoms survive the strong UV radiation (Visser et al. 2007). For this analysis three abundance values are considered, 1% 10% and 50% with respect to the abundance of the interstellar medium (Draine & Li 2007). The gas-to-dust mass ratio (Δ_{gd}) in disks is likely to be lower than that of the interstellar medium (e.g. Chapillon et al. 2010). In this paper Δ_{gd} varies between 1% and 100% the ISM value (Bohlin et al. 1978).

The effects of elemental carbon abundance and isotope selective photodissociation (relevant for ^{13}CO) are not treated here. These are investigated in Bruderer et al. (2012) and Miotello et al. (2014). As noted by Miotello et al. (2014), the ^{13}CO line intensities are less affected by the isotope selective photodissocia-

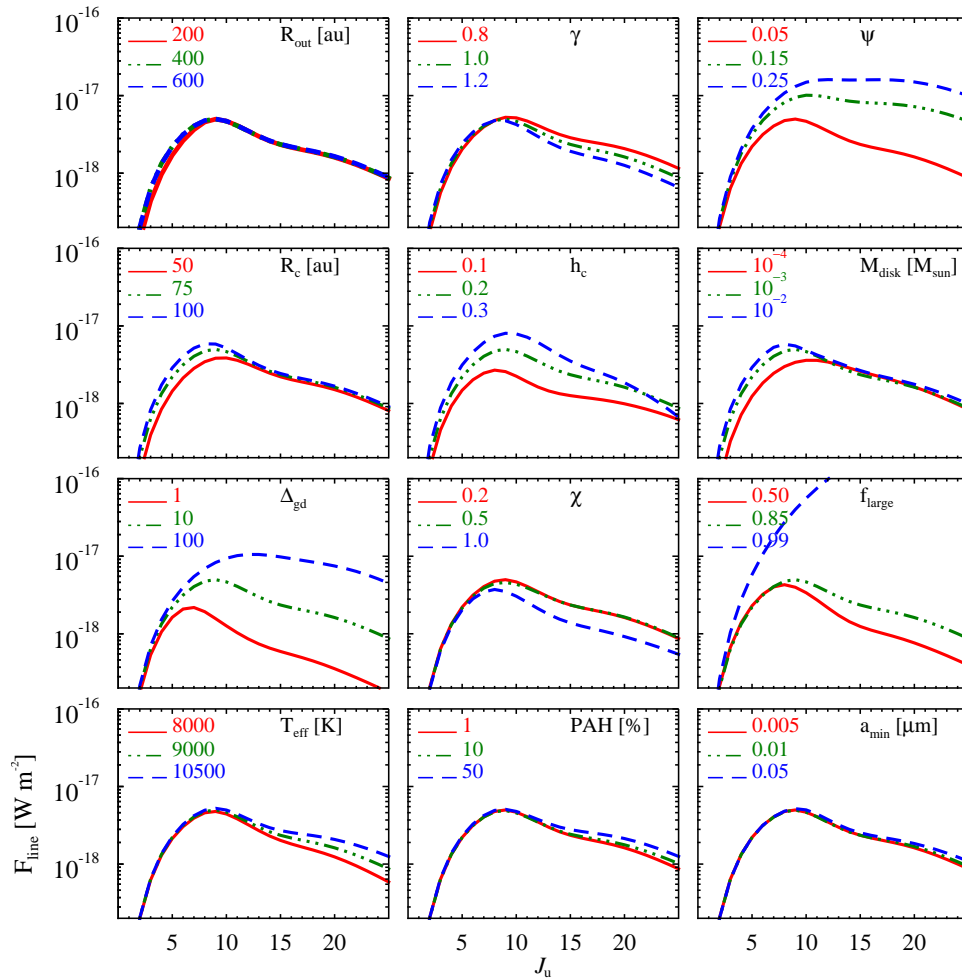


Fig. 6. Synthetic CO ladder for different disk parameters (see Table 3). Fluxes measured assuming a distance of 100 pc and a disk inclination of 45° .

tion compared to C^{18}O and C^{17}O . It is thus reasonable to neglect this effect in this analysis. The effect of a lower carbon abundance is similar to that of a smaller gas-to-dust ratio (Bruderer et al. 2012).

5.2. Temperature radial gradient

Figure 5 shows the T_{gas} radial profile for all disk models: each panel shows the temperature gradient in the disk midplane ($z/r = 0.01$) and at $z/r = 0.6$, representative of the CO emitting layer. In the case of $h_c = 1$, the CO emitting layer is $z/r \sim 0.2 - 0.3$ and the dash-dotted line shown in Figure 5 shows the temperature gradient at $z/r = 0.3$.

The parameters affecting most the midplane temperature are the flaring angle, scale height, the dust settling and to a lesser extent the disk mass and the gas-to-dust mass ratio. At the CO emitting layer the temperature gradient is controlled mostly by the disk flaring and to a less extent by the disk mass, the gas-to-dust mass ratio, the dust settling (f_{large}) and by the stellar temperature. Note that the $f_{\text{large}} = 0.999$ case is a very extreme scenario in which the disk outer layers are almost completely devoid of dust as the

bulk of the mass is the large dust grains, which are settled in the disk midplane ($\chi = 0.2$).

5.3. CO line fluxes

The synthetic CO ladders are shown in Figures 6. In all cases the distance is fixed to 100 pc and the disk inclination to 45° .

There are two main aspects of the CO ladder that the models need to reproduce: the absolute line fluxes and the shape of the CO ladder, in particular whether or not it bends over at higher J . No changes are observed for different disk size. The parameter that affects primarily the CO line ladder are:

Flaring angle : the CO line fluxes vary by 1-2 order of magnitude between the flat (fainter) and the flared disks for $J \gtrsim 10$ and the line flux difference increases with J . This is due to the different gas temperature structure between flat and flared disks (Figure 5)

Critical radius : the low- J ($J < 10$) lines become brighter with R_c while the flux of the high- J does not vary. Since the temperature structure does not vary with R_c (Figure 5), this

is likely due to the change in vertical depth in the outer disk due to the change in R_c

Scale height : all CO lines become brighter if the scale height increases. Since the temperature radial gradient does not show significant changes with h_c (at the CO emitting layer), the differences in CO line fluxes are due to shift of the $C^+/C/CO$ transition layers deeper into the disk with decreasing scale height

Disk mass : it affects the low- J ($J < 10$) lines only which become slightly brighter for increasing disk mass. The effect is only significant for low disk masses ($\lesssim 10^{-4} M_\odot$) and it is due to the change in gas column density (hence line optical depth) in the outer disk

Gas-to-dust mass ratio : reducing Δ_{gd} from 100 to 1 has the effect of lowering all line fluxes by up to one order of magnitude. Note that keeping the gas mass constant and lowering the gas-to-dust mass ratio implies a higher dust mass. Thus the CO lines are fainter for low values of Δ_{gd} because of the increased opacity and lower temperature (Figure 5) induced by the higher dust mass compared to the $\Delta_{gd} = 100$ case

Dust settling and large-to-small grains mass ratio : the high- J lines are brighter for a settled disk and for an higher mass ratio. This is due to the increase in gas temperature in the disk upper layers. In the extreme case of $f_{large} = 0.999$ all the CO lines are several order of magnitudes brighter.

All other remaining parameters analysed here affect mostly the flux of the high- J ($J \gtrsim 10$) lines inducing a bending over the CO ladder for $J \gtrsim 10$.

For comparison, Figure 7 shows the CO ladder in the case of a “cold” disk atmosphere (i.e. $T_{gas} = T_{dust}$, obtained by switching off the thermal balance in DALI). In this case all the CO line fluxes are substantially lower and the flux drops quickly with J for $J_u \gtrsim 10$. The shape of the observed CO ladder and the absolute flux level are inconsistent with the cold disk case, thus suggesting that T_{gas} exceeds T_{dust} in the upper layers of all the Herbig Ae disks studied here.

The ^{13}CO ladder is shown in Figure 8 for two representative disk models. The fluxes of the ^{13}CO lines in the PACS range are all below the detection threshold of the DIGIT and GASPS surveys. The estimate of the ^{13}CO $J = 10 - 9$ flux is in good agreement (once corrected for distance) with the value measured in this paper for HD 100546 and HD 163296 (Table 1). The fluxes of the mid- J ^{13}CO lines reported by van der Wiel et al. (2014) toward HD 100546 (based on Herschel/SPIRE) are much brighter than the values estimated here. As noted by van der Wiel et al. (2014) the SPIRE measurements may be contaminated by an extended, non-disk, emission.

As shown by the line contribution function in Figure 4, the ^{13}CO emission probes a layer closer to the disk midplane at smaller distance to the star compared to the ^{12}CO emission. The relative fluxes and line profiles of multiple high- J transitions of the two isotopologues provide a strong constraint to the disk temperature structure both in the radial and in the vertical direction.

Finally, Figure 9 shows the effect of a dust gap in the CO ladder for the flared ($\psi = 0.25$) disk case: a dust gap is included between 1–13 au with a drop in dust surface density of $\delta_{dust} = 10^{-6}$

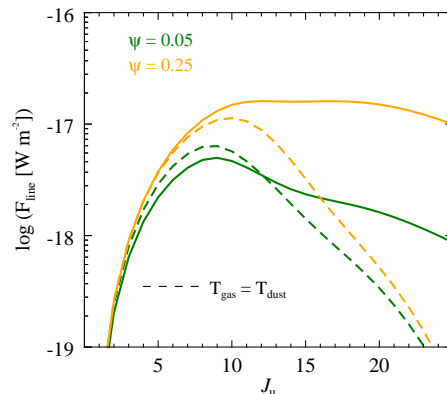


Fig. 7. Synthetic CO ladder in the case of $T_{gas} = T_{dust}$ case (representative models only).

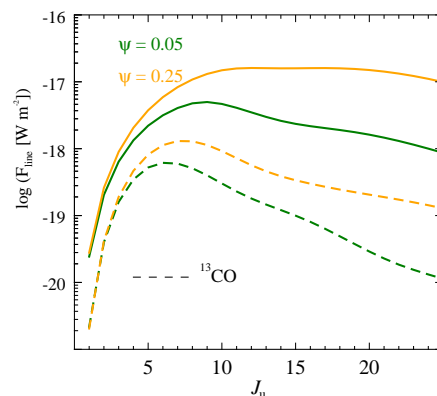


Fig. 8. Synthetic ^{13}CO ladder (representative models only).

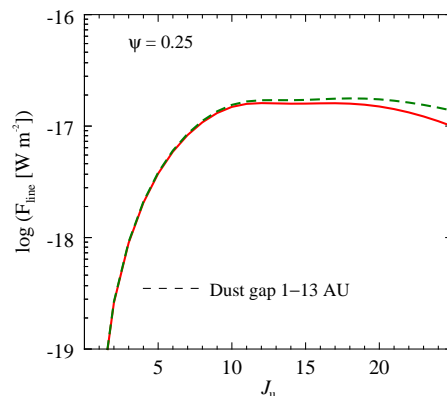


Fig. 9. Synthetic CO ladder for the flared disk case ($\psi = 0.25$) with (dashed, green curve) and without dust gap.

and a drop in the gas surface density $\delta_{gas} = 10^{-6}$. Such a structure is representative of the Herbig Ae group I systems analyzed here (e.g., HD 100546). As the figure shows, the dust gap does not impact the CO ladder for $J < 25$. This is because the high- J lines analysed here are emitted at radii larger than the dust gap.

5.4. CO line profiles

The predicted velocity profiles of different CO transitions are shown in Figure 10 (^{13}CO) for the representative models. A mix of low- and high-*J* transitions are plotted for a disk inclination of $i = 45^\circ$. In all cases the line width increases with *J*. The larger differences in line width are seen for the flat disk models. Note that these differences in line width become particularly significant for $J = 16 - 15$, not yet for $J = 10 - 9$, demonstrating the power of these high-*J* HIFI data. For $\psi = 0.05$ the disk scale height and the dust settling have only minor effect on the line velocity profiles. In the case of $\psi = 0.25$ instead, all the lines become broader if there is substantial dust settling while changing the scale height from $h_c = 0.2$ to 0.3 has little impact (not shown here).

The ^{13}CO lines are systematically broader than the ^{12}CO lines (Figure 10) and this is particularly true for the higher *J* transitions. This is because the ^{13}CO transitions become optically thick at higher density and the line emitting region moves deeper into the disk and closer to the star (for a given *J*) compared to the ^{12}CO transitions. This can be seen in Figure 4 which shows the gas density structure and the line contribution function.

6. Discussion and conclusion

The major finding of this paper is that the disk temperature structure varies substantially from system to system (Figure 3). This result is based on the analysis of the high-*J* CO line profiles and of the CO rotational ladder. Note in particular that the 4 Herbig Ae systems have similar stellar mass ($M_\odot \sim 2 - 2.5 M_\odot$) while the disk temperature can differ by almost an order of magnitude. The comparison of the observed (Figure 2) and synthetic (Figure 6) CO ladders suggest a disk temperature sequence for the 4 Herbig Ae systems studied here (when accounted for the different distances of the sources). In this sequence HD 100546 is the hottest and HD 163296 the coldest disk. The primary parameters regulating the overall disk temperature are the flaring angle, the scale height and the gas-to-dust mass ratio; varying these parameters induce variation of the CO line flux up to 1-2 order of magnitude. The disk temperature structure is sensitive to the disk mass only for $M_{\text{disk}} \lesssim 10^{-4} M_\odot$. Dust settling may also lead to changes in the disk temperature. The power-law exponent of the surface density profile, the stellar temperature and PAH abundance have secondary effects on the temperature of Herbig Ae disks affecting mostly the CO ladder shape, producing a bending in the CO rotational ladder for $J \gtrsim 10$. In some cases, changes in the CO ladder are not due to a different temperature structure (Sec. 5.3): as an example, a different disk critical radius affects the value of the low-*J* CO lines ($J < 10$) while the overall temperature structure does not vary substantially.

An interesting outcome of the analysis performed here is that the CO ladder may help to constrain some key physical parameters in disks like the gas-to-dust mass ratio, or equivalently the elemental carbon abundance (Bruderer et al. 2012). Spatially-resolved millimetre images of the low-*J* lines allow to accurately measure the disk flaring angle and scale height (de Gregorio-Monsalvo et al. 2013) while multi-frequency dust continuum observations provide strong constraints on the grain size distribution reducing the degeneracy in the CO ladder. Once these properties are measured, the major differences in the CO ladder are driven by the gas-to-dust mass ratio.

In conclusion, the CO rotational ladder and the velocity profiles of multiple-*J* transitions are a valid diagnostic of T_{gas} in disks.

With the end of *Herschel* operation, the investigation of the far-infrared spectrum of disks is currently limited to the very bright sources observable with SOFIA. Future observations with, e.g., cryogenic facilities like SPICA will allow to expand the analysis of the CO (and isotopologues) rotational ladder to a much larger sample of protoplanetary systems allowing to routinely measure the temperature structure of not only flared but also flat Herbig AeBe and T Tauri disks. In particular, the line flux ratio of several, mid- and high-*J* CO and ^{13}CO will provide direct insights on the vertical (different τ) and radial (different *J*) temperature structure of protoplanetary disks if complemented by lower-*J* spectrally and spatially resolved data from, e.g., ALMA.

Acknowledgements. DF acknowledges support from the Italian Ministry of Science and Education (MIUR), project SIR (RBSI14ZRHR). The authors thanks the WISH team and L. Podio for providing the HIFI ^{12}CO and $^{13}\text{CO } J = 10 - 9$ spectra of TW Hya and HD 163296. We are also grateful to the DIGIT, GASPS teams for providing the PACS spectra of CO. Astrochemistry in Leiden is supported by the Netherlands Research School for Astronomy (NOVA), by a Royal Netherlands Academy of Arts and Sciences (KNAW) professor prize, and by the European Union A-ERC grant 291141 CHEMPLAN.

References

- Andrews, S. M., Wilner, D. J., Espaillat, C., et al. 2011, *ApJ*, 732, 42
 Bast, J. E., Brown, J. M., Herczeg, G. J., van Dishoeck, E. F., & Pontoppidan, K. M. 2011, *A&A*, 527, A119
 Bergin, E. A., Cleeves, L. I., Gorti, U., et al. 2013, *Nature*, 493, 644
 Bohlin, R. C., Savage, B. D., & Drake, J. F. 1978, *ApJ*, 224, 132
 Brittain, S. D., Najita, J. R., & Carr, J. S. 2009, *ApJ*, 702, 85
 Brown, J. M., Pontoppidan, K. M., van Dishoeck, E. F., et al. 2013, *ApJ*, 770, 94
 Bruderer, S. 2013, *A&A*, 559, A46
 Bruderer, S., van der Marel, N., van Dishoeck, E. F., & van Kempen, T. A. 2014, *A&A*, 562, A26
 Bruderer, S., van Dishoeck, E. F., Doty, S. D., & Herczeg, G. J. 2012, *A&A*, 541, A91
 Chapillon, E., Parise, B., Guilloteau, S., Dutrey, A., & Wakelam, V. 2010, *A&A*, 520, A61
 D'Alessio, P., Calvet, N., Hartmann, L., Franco-Hernández, R., & Servín, H. 2006, *ApJ*, 638, 314
 de Gregorio-Monsalvo, I., Ménard, F., Dent, W., et al. 2013, *A&A*, 557, A133
 Dent, W. R. F., Thi, W. F., Kamp, I., et al. 2013, *PASP*, 125, 477
 Draine, B. T. & Li, A. 2007, *ApJ*, 657, 810
 Dutrey, A., Guilloteau, S., Prato, L., et al. 1998, *A&A*, 338, L63
 Fedele, D., Bruderer, S., van den Ancker, M. E., & Pascucci, I. 2015, *ApJ*, 800, 23
 Fedele, D., Bruderer, S., van Dishoeck, E. F., et al. 2013a, *A&A*, 559, A77
 Fedele, D., Bruderer, S., van Dishoeck, E. F., et al. 2013b, *ApJ*, 776, L3
 Geers, V. C., Augereau, J., Pontoppidan, K. M., et al. 2006, *A&A*, 459, 545
 Gorti, U. & Hollenbach, D. 2008, *ApJ*, 683, 287
 Green, J. D., Evans, II, N. J., Jørgensen, J. K., et al. 2013, *ApJ*, 770, 123
 Jonkheid, B., Dullemond, C. P., Hogerheijde, M. R., & van Dishoeck, E. F. 2007, *A&A*, 463, 203
 Kamp, I., Thi, W.-F., Meeus, G., et al. 2013, *A&A*, 559, A24
 Kamp, I., Tilling, I., Woitke, P., Thi, W.-F., & Hogerheijde, M. 2010, *A&A*, 510, A18
 Koerner, D. W. & Sargent, A. I. 1995, *AJ*, 109, 2138
 Mannings, V. & Sargent, A. I. 1997, *ApJ*, 490, 792
 Meeus, G., Montesinos, B., Mendigutía, I., et al. 2012, *A&A*, 544, A78
 Meeus, G., Salyk, C., Bruderer, S., et al. 2013, *A&A*, 559, A84
 Miotello, A., Bruderer, S., & van Dishoeck, E. F. 2014, *A&A*, 572, A96
 Panić, O., van Dishoeck, E. F., Hogerheijde, M. R., et al. 2010, *A&A*, 519, A110
 Pontoppidan, K. M., Blake, G. A., & Smette, A. 2011, *ApJ*, 733, 84
 Pontoppidan, K. M., Boogert, A. C. A., Fraser, H. J., et al. 2008, *ApJ*, 678, 1005
 Qi, C., D'Alessio, P., Öberg, K. I., et al. 2011, *ApJ*, 740, 84
 Roelfsema, P. R., Helmich, F. P., Teyssier, D., et al. 2012, *A&A*, 537, A17
 Salyk, C., Pontoppidan, K., Corder, S., et al. 2014, *ApJ*, 792, 68
 Sturm, B., Bouwman, J., Henning, T., et al. 2010, *A&A*, 518, L129
 van den Ancker, M. E., de Winter, D., & Tjin A Dije, H. R. E. 1998, *A&A*, 330, 145
 van der Plas, G., van den Ancker, M. E., Acke, B., et al. 2009, *A&A*, 500, 1137
 van der Wiel, M. H. D., Naylor, D. A., Kamp, I., et al. 2014, *MNRAS*, 444, 3911
 van Kempen, T. A., Kristensen, L. E., Herczeg, G. J., et al. 2010, *A&A*, 518, L121
 van Zadelhoff, G., van Dishoeck, E. F., Thi, W., & Blake, G. A. 2001, *A&A*, 377, 566
 Visser, R., Geers, V. C., Dullemond, C. P., et al. 2007, *A&A*, 466, 229
 Woitke, P., Kamp, I., & Thi, W. 2009, *A&A*, 501, 383

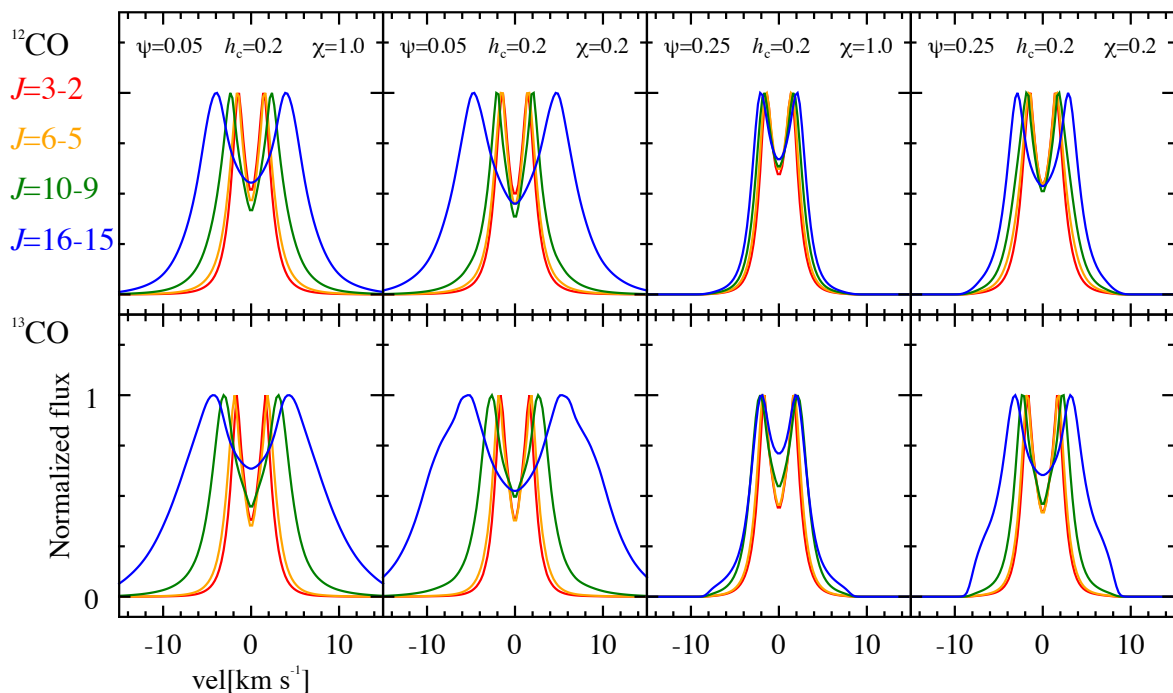


Fig. 10. CO (top) and ^{13}CO (bottom) line profiles computed with DALI as a function of dust settling and flaring angle for a disk inclination of $i = 45^\circ$. The remaining parameters are fixed: $h_c=0.2$, $\Delta_{\text{gd}} = 100$, $T_{\text{eff}} = 10, 500$ K, $\text{PAH}=1\%$, $f_{\text{large}} = 0.85$.

Appendix A: CO Rotational Ladder

The fluxes of the CO rotational lines up to $J = 25 - 24$ are listed in Table A.1. Data are from this work and from Bergin et al. (2013); Bruderer et al. (2014); Fedele et al. (2013b); Kamp et al. (2013); Meeus et al. (2013); Qi et al. (2011); van der Wiel et al. (2014) (and references therein) and from Kama et al. (submitted). The flux of the $J = 6 - 5$ in IRS 48 is a lower limit because the line is partially obscured by the molecular cloud (Bruderer et al. 2014). Some of the high- J line fluxes ($J > 14 - 13$) based on *Herschel*/PACS observations have been re-measured with the most updated instrument's calibration and some of the fluxes are slightly different than previous measurements. The $J = 24 - 23$ in TW Hya is blended with $\text{H}_2\text{O } 4_{14} - 3_{03}$.

Appendix B: [C II]

[C II] emission is detected at high S/N toward both sources (HD 97048 and HD 100546, Figure B.1). The line is narrow with a Gaussian FWHM of $\sim 3 - 4$ km s $^{-1}$. In the case of HD 97048 the peak of the emission is at $v_{\text{LSR}} \sim 5.1$ km s $^{-1}$, red-shifted from the center of the CO $J = 16 - 15$ line by ~ 0.2 km s $^{-1}$.

The analysis of the [C II] profile toward HD 100546 is presented in paper I and the spectrum is shown here for comparison with that of HD 97048. Because of the internal load chop used in combination with an off-source calibration with HIFI, some of the large scale line emission is removed in the HIFI spectra. Given the large beam of HIFI at this frequency ($11''1$), the large-scale, non-disk, emission contributes most of the [C II] flux and we conclude that the emission measured here is dominated by a diffuse, low-velocity gas not associated with the disk, i.e., diffuse cloud or remnant envelope on scales of 1000 au.

In the case of HD 100546, the base of the [C II] line is broader than the core of the line as can be seen from the high velocity

wings. This broadening may be due to an underlying disk contribution. To quantify this, the line wings are fitted with a Gaussian profile centered at the system velocity ($V_{\text{LSR}} = 5.6$ km s $^{-1}$). The best fit profile is shown in Figure 1 (red curve). The fit is partly degenerate in the Gaussian height and width. Nevertheless, in order to fit the high velocity wings, the FWHM must range between $\sim 7 - 8$ km s $^{-1}$. The disk [C II] contribution is estimated by integrating the flux below the best-fit Gaussian profile and we find a value of $\sim 8 - 9 \times 10^{-17}$ W m $^{-2}$, correspondent to 4-5% of the total line flux. This value must be taken with caution for various reasons (e.g., the intrinsic line profile is not Gaussian).

No evidence of line broadening is detectable in the HIFI [C II] spectrum of HD 97048. The upper limit to the [C II] disk contribution is measured assuming a line peak equal to 0.3 K ($3 \times \text{rms}$, Table 1) and a line width of 7 km s $^{-1}$ (similar to HD 100546). This gives a 3σ upper limit of 2.4 K km s $^{-1}$ equivalent to 5.5×10^{-17} W m $^{-2}$.

Appendix C: Spectral energy distribution of representative models

The Spectral energy distribution of the two representative disk models is shown in Figure C.1.

Table A.1. CO rotational ladder fluxes

	TW Hya	HD 97048	HD 100546	IRS 48	HD 163296
	Integrated Flux [10^{-17} W m $^{-2}$]				
2-1	0.014 ± 0.0007				0.035 ± 0.00039
3-2	0.043 ± 0.0013		0.15 ± 0.01		0.125 ± 0.00130
4-3					
5-4					1.04 ± 0.40
6-5	0.13 ± 0.03	0.63 ± 0.03	1.3 ± 0.1	> 0.17	0.74 ± 0.29
7-6		0.8 ± 0.4			0.90 ± 0.30
8-7		1.8 ± 0.8			1.24 ± 0.55
9-8		2.4 ± 0.5			0.91 ± 0.40
10-9	0.28 ± 0.06	3.5 ± 0.7	4.5 ± 0.1		1.17 ± 0.35
11-10		3.6 ± 0.7			1.13 ± 0.35
12-11		2.8 ± 0.6			1.17 ± 0.35
13-12		4.9 ± 0.9			1.52 ± 0.40
14-13		2.4 ± 1.4	8.5 ± 1.0	< 1.8	< 1.60
15-14		3.0 ± 0.8	6.9 ± 1.0	1.3 ± 0.5	1.03 ± 0.50
16-15		3.0 ± 0.5	5.6 ± 1.0	1.6 ± 0.4	< 1.30
17-16		2.6 ± 0.5	7.1 ± 1.0	1.7 ± 0.4	0.75 ± 0.25
18-17	0.30 ± 0.10	2.6 ± 0.5	5.8 ± 1.0	1.3 ± 0.3	< 0.90
19-18		< 2.3	7.4 ± 1.0	1.1 ± 0.4	< 0.90
20-19		< 2.3	5.2 ± 1.0	1.2 ± 0.4	< 0.90
21-20		< 2.3	8.6 ± 1.0	1.0 ± 0.3	< 0.90
22-21		< 2.3	7.3 ± 1.0	< 1.4	< 0.90
23-22	< 0.44	< 2.3	7.8 ± 1.1	< 1.3	< 0.90

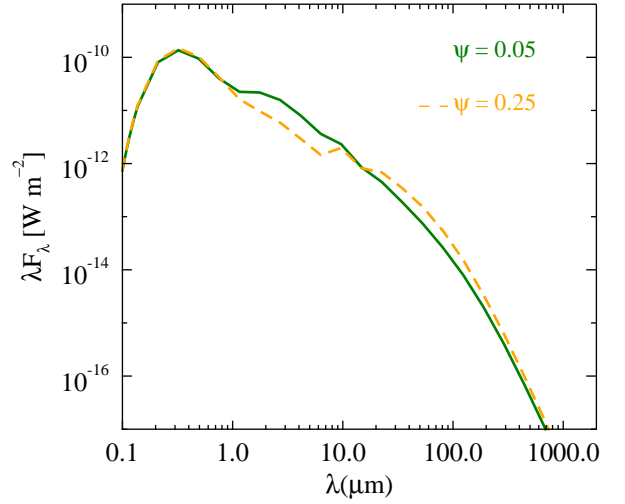
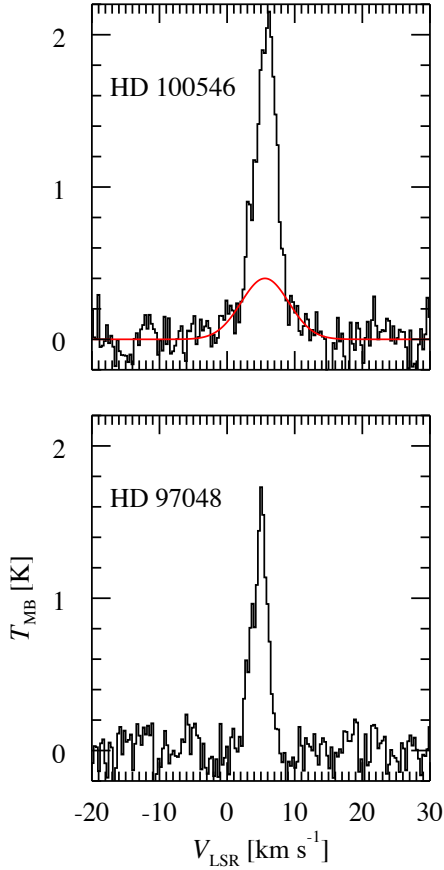

Fig. C.1. Spectral energy distribution of the two representative disk models.

Fig. B.1. HIFI/WBS spectra of [C II]. The base of the [C II] line in HD 100546 is fitted with a Gaussian profile (red curve).